Simulating the Tumor Microenvironment for Immune Cell Interactions via Deployable Extrusion Bioprinting

Corrado Mazzaglia*[1], Yaqi Sheng*[2,3], Leonor Nunes Rodrigues [1], Iek Man Lei [3], Jacqueline D. Shields [1,4] and Yan Yan Shery Huang [2,3]

[1] MRC Cancer Unit, University of Cambridge, Cambridge, UK

[2] The Nanoscience Centre, University of Cambridge, Cambridge, UK

[3] Department of Engineering, University of Cambridge, Cambridge, UK

[4] Comprehensive Cancer Centre, King's College London, Great Maze pond, London, UK

* Authors have equal contributions

Correspondence: Jacqueline.Shields@kcl.ac.uk; yysh2@cam.ac.uk

Keywords: tumoroids, TME, bioprinting, CAFs, immune, immunotherapy

Abstract

Three-dimensional (3D) bioprinting has emerged as a promising tool for constructing tumor microenvironments (TME) for cancer modelling *in vitro*. Realizing the translational impacts of 3D bioprinting for cancer research necessitates innovation in bioprinting workflows which integrate affordability, user-friendliness, and biological relevance. Herein, we demonstrate 'bioArm', a simple, yet highly effective extrusion bioprinting platform, which can be folded into a carry-on pack, and rapidly deployed between bio-facilities. BioArm enabled TME reconstruction in the form of 3D core-shell tumoroids with cancer-associated fibroblasts (CAFs). Tumoroids showed the presence of a heterogenous population of CAFs with de novo synthesized extracellular matrices, demonstrating more *in vivo*-like characteristics compared to conventional 2D co-culture models. Embedding the 3D printed tumoroids in an immune

cell laden collagen matrix permitted tracking of the interaction between immune cells and tumoroids, and subsequent immunotherapy treatments. Our deployable extrusion bioprinting workflow could significantly widen the accessibility of 3D bioprinting for gaining mechanistic understanding in TME, and for developing strategies in cancer drug testing.

1 Introduction

Cancer remains one of the leading causes of death worldwide, accounting for 10 million deaths in 2020 [1]. Despite the collective effort to improve the quality of therapies and patients' life, the number of cases are increasing yearly, expecting a 47% rise of new cases by 2040 (Sung et al., 2021). Current standard of care treatments include surgery, chemotherapy and radiotherapy, but in recent years a significant effort has been directed towards developing novel therapeutic platforms. The emergence of immunotherapies, which target and engage the immune system to fight cancer, have revolutionized cancer treatment, improving survival of cancer patients with advanced disease. Yet despite this promise, a large proportion of patients do not respond or develop resistance. Thus, there remains a need to understand the mechanisms of action of therapies, and appropriate models in which to perform studies.

The tumor microenvironment (TME) is host to multiple cell types – fibroblasts, blood and lymphatic endothelial cells, pericytes and immune cells - which together support disease progression [3]. The heterogeneity of this *niche* likely contributes to the variability of treatment responses observed, through complex interactions that remain to be determined [4]. To help model disease and elucidate cytotoxic mechanisms of action induced by anti-tumor therapies, the use of *in vitro* systems has proven invaluable [5], [6]. With our increasing understanding of the complexities of the tumor, *in vitro* models for TME have evolved from two-dimensional co-cultures on tissue-culture plastic to more sophisticated systems whereby cells were grown in 3D environments in both matrix or matrix-free contexts [7], [8], [9], [10], [11]. The development of such cancer models with TME has helped to reveal that manner in which a cell is cultured can result in altered gene and protein expression [12], [13] dramatically influencing data interpretation and conclusions[14]. These 'new-age' *in vitro* TME models are advantageous in that they are tractable, enabling researchers to readily manipulate, visualize, and even

perform long-term experiments. They are also more cost-effective and ethical, compared to *in vivo* models.

Afforded by the ability to position cells and materials precisely and reproducibly, 3D bioprinting has been shown as an invaluable tool to construct *in vitro* cancer models, especially relevant to the multi-compartmental nature of TME [15], [16], [17]. Compared to the various 3D bioprinting techniques, extrusion bioprinting has unique strengths of supporting flexible multi-material and high cellular density (i.e. ~10^8 cells/ml) deposition, with efficient usage of precious biological materials. However, ongoing innovations in bioprinting for reconstructing TME *in vitro* need to overcome several barriers, including high costs and limited adaptability associated with commercial systems [18], [19]; and the lack of fit-for-purpose demonstrations for cancer modelling associated with open-design platforms. Moreover, most existing bioprinters are designed on permanent fixtures, which are difficult relocated or reassembled. This causes problems when printing inside small hoods, or switching between working spaces when the biological materials are nontransportable due to materials transfer agreement or ethical restrictions. Although portable handheld extruders have recently been reported [20]; [21], the needs for manual control of extruder movements largely compromised the printing accuracy and reproducibility for *in vitro* model.

To overcome the above limitations, we developed a deployable, extrusion 3D bioprinter, termed bioArm, based on a custom-built printhead and a hackable robotic arm. Apart from its low-cost (< £900), small (18x35x37cm) and lightweight (around 5kg) features, bioArm was designed to be foldable into a portable format (Figure 1A) for easy of storage and transportation. Here, we show that this deployable bioprinter can perform rapid and reproducible manufacture of 3D tumoroids incorporating TME components. Inclusion of cancer-associated fibroblasts (CAFs) supports ECM deposition and immune cell recruitment. We then applied immunotherapy to perturb the system, showing enhanced immune motility and recruitment. While we tested immunotherapy, this platform has potential to screen a wide range of tumor therapies and monitor the therapeutic response in not only tumor cells, but also in the adjacent stroma.

2 Materials and Methods

Printer set-up

An in-house built deployable, extrusion-based bioprinter was used for tumoroids printing inside the biosafety cabinet. The portable bioprinter consists of a stepper motor (RS PRO Hybrid Stepper Motor 1.8°) driven printhead controlled by Arduino (Arduino Mega 2560), a robotic arm (uArm Swift Pro, UFactory, accuracy 0.2 mm) controlled by Python codes, and necessary supporting metal frames [22].

To conduct 3D bioprinting experiments, a PLA-based stage designed using Autodesk Inventor was printed using Ultimaker 3. The stage was attached to the robotic arm to hold the Petri dish, which then moved along defined printing path once the home-written Python code was actuated on a computer. During the robotic arm movement, bio-ink, which is in this case a cell-laden hydrogel, was extruded from the printhead to form desired constructs on the petri dish.

Cell culture

mM1 murine pancreatic ductal adenocarcinoma cells isolated from KPC tumors (kind gift of Dave Tuveson, CSHL) were maintained in DMEM culture media supplemented with FBS 10% and 5% penicillin-streptomycin. Pancreatic cancer associated fibroblasts (PanCAFs) previously isolated from KPC tumor-bearing mice [23] were maintained in RPMI media supplemented with FBS 10% and 5% penicillin-streptomycin and 10mM 4-(2-hydroxyethyl)-1-piperazineethanesulfonic acid (HEPES) at 37C and 5% CO_2 humidified atmosphere.

In vitro to *in vivo* comparison

Immune and CAF phenotypes from tumoroids were compared with *in vivo* tumors. Mice were used in accordance with the UK Animals in Science Regulation Unit's Code of Practice for the Housing and Care of Animals Bred, Supplied or Used for Scientific Purposes, the Animals (Scientific Procedures) Act 1986 Amendment Regulations 2012. All procedures were performed under a UK Home Office Project license (PPL P88378353), which was reviewed and approved by the Medical research Council Laboratory of Molecular Biology Animal Welfare and Ethical Review Bodies (AWERB). Mice were socially housed in individually ventilated cages, at ambient temperature and with cage enrichment. To induce tumours, $1x10^6$ mM1 pancreatic tumors cells were injected subcutaneously into the flank of immune competent C57/Bl6 mice bred in house. Mice were monitored daily, and tumor size

measured non-invasively with digital calipers. Animals were euthanized by exposure to CO_2 followed by cervical dislocation at days 7 and 11, and samples prepared for flow cytometry. Briefly, tumors were minced using a razor and digested with 1mg/ml collagenase A and collagenase D and 0.4mg/ml DNase I in PBS at 37°C for 2h with rotation at 600rpm in a thermomixer compact (Eppendorf). 10mM EDTA was then added to stop the enzymatic reaction. The resulting cell suspension was passed through a 70µm filter ready for antibody staining.

Immune cell isolation

Spleens of WT C57/bl6 mice or C57BL/6-Tg(CAG-EGFP)131Osb/LeySopJ (CAG.egfp, stock number 006567, Jax labs) mice were mechanically disrupted. Red blood cells were lysed with RBC lysis buffer (155mM NH_4Cl, 12mM $NaHCO_3$ and 0.1mM EDTA in ddH2O) for 5 minutes at RT, then neutralized with excess media. After centrifugation at 1500rpm 5 mins, samples were resuspended and passed through a 70µm cell strainer to obtain a single cell suspension. Cells were maintained in RPMI media containing IL-4 (20ng/ml, Peprotech 214-14) and IL-7 (10ng/ml, Peprotech 217-17) for the duration of experiments.

Cell-laden gel preparation for tumoroid printing

For tumoroid printing, the hydrogel was prepared by dissolving 6%(w/v) gelatin powder (G1890, Sigma-Aldrich) and 1% sodium alginate powder (W201502, Sigma-Aldrich) in PBS and was stirred at 60°C until transparent. The hydrogel was then sterilized using 0.22µm filter (1181465, Camlab) and kept at 37°C in an incubator before mixing with cells. MM1 cells and PanCAFs in a 3:1 ratio was used for the cancer compartment, and PanCAFs only were used for the stromal compartment. After trypsinisation, the cells for each compartment were combined according to the above ratio, centrifuged at 1500 rpm, and resuspended in hydrogel at 37°C to a final concentration of $1.7x10^8$ cells/ml unless otherwise stated. The cell-laden gels for each compartment were then transferred into 1ml luer-lock syringes at 37°C and fitted with 25 Gauge needles. The syringes were kept at 4°C for 20 minutes to enable thermo-gelation before printing.

Tumoroid printing and post-printing treatments

Immediately prior to printing, syringes containing cell-laden gels were wiped using 70% ethanol to avoid contamination. To generate the core-shell structure, the syringe filled with

the stromal compartment (CAFs) was first fitted in the printhead to print up to 6 structures (dimension around: 2mm x 2mm x 2mm) directly on a 35mm petri-dish The syringe was then changed to print the tumor cell compartment (dimension around: 1mm x 1mm x 1mm) inside each stromal structure sequentially. The above printing process was repeated until the required number of tumoroids was printed. To crosslink alginate in the printed tumoroids, 104 mM $CaCl_2$ (C5670, Sigma-Aldrich) in sterile PBS solution was prepared and passed through a 0.22µm filter. For each 35mm petri-dish with up to 6 printed tumoroids, 3 ml of 104 mM $CaCl_2$ solution was added and was then replaced with culture medium after 2 minutes of incubation at room temperature. After crosslinking, tumoroids were manually transferred into 12-well culture plates coated with a layer of 2% (w/v) agarose (A9539, Sigma-Aldrich) gel. 48 hours after printing, alginate was removed by treating structures with Alginate Lyase (A1603, Sigma-Aldrich) which was added to the culture medium (DMEM and RPMI-1640 1:1 ratio). The enzyme solution was removed after 24 hours, and media was exchanged daily until testing.

Flow cytometry

Cell suspensions were resuspended in PBS with Live/Dead Fixable Violet (Thermo, Cat: 62248) viability dye, diluted 1:1000, for 15 minutes. After washing, samples were incubated with fluorophore-conjugated primary antibodies prepared at 1:300 dilution in FACS buffer (0.5% Bovine Serum Albumin or 'BSA' in PBS and mixed 1:1 with Fc blocker (generated in house from a rat 2.4G2 hybridoma cell line)), for 40 minutes, at 4°C. Primary antibodies for CAFs: anti-PDPN (Biolegend 127417, APC-Cy7 conjugated), anti-PDGFRα (Biolegend 135911, Pe-Cy7 conjugated), anti-αSMA (Invitrogen 41-9760-82, eFluor 570 conjugated) and anti-CD34 (Invitrogen 50-0341-82, conjugated eFluor 660). Primary antibodies for immune profiling: anti-B220 (Biolegend 103224, APC-cy7 conjugated), anti-CD4 (Invitrogen 25-0041-82, PE-Cy7 conjugated), anti-CD8a (Invitrogen 47-0081-80, APC conjugated), anti-cd11b (Biolegend 101208, PE conjugated) After surface staining, if intracellular epitope detection was required, samples were fixed and stained in accordance with the FoxP3/ Transcription Factor Staining Kit (eBioscience, Cat: 00-5523). Cells were incubated with fluorophore-conjugated primary antibodies, diluted 1:300 in permeabilization buffer, for 30 minutes at room temperature. After washing, samples were run on an LSR Fortessa cell analyzer (BD Biosciences) and analysed using FlowJo version 10. (FlowJo, BD Biosciences).

Confocal imaging

Tumoroids were harvested and embedded in OCT (optimal cutting temperature compound) for cutting into 10µm sections. Tissue sections were then air dried and fixed in a 1:1 mix of acetone and methanol, for 2 minutes at -20°C. Sections were then washed in PBS, for 10 minutes before incubation in blocking solution containing 10% chicken serum for 1 hour, at room temperature. Samples were then incubated with primary antibodies against PDGFRα (Goat IgG, R&D systems AF1062), Collagen I (Rabbit IgG, Biorad 2150-1410), Perlecan (Rat IgG, Invitrogen MA1-06821) and Osteopontin (Goat IgG, R&D systems AF808) diluted in blocking buffer, at 4°C, overnight. For immune cells detections the tumoroids sections also were incubated overnight at 4°C with anti-B220 (Biolegend 103224, APC-cy7 conjugated) and anti-cd11b (Biolegend 101208, PE conjugated). Following 3 x 5 mins washes in PBST (PBS with 0.1% Tween), sections were incubated with 1:300 Chicken anti-Rat Conjugated AF488 (A21471), Donkey anti-Rabbit conjugated AF594 (A21207) and Chicken anti-Goat conjugated AF647 (A21469) for 1 hour, at room temperature. Sections were then counterstained with 1µg/ml of 4',6-diamidino-2-phenylindole (DAPI, Thermo, D1306), for 10 minutes, and mounted with 22 x 50 mm glass coverslips and SlowFade Gold Antifade Mountant (Life Technologies; Cat: S36936). Sections were imaged on a Leica SP5 laser scanning confocal microscope using a 10x and 40x oil objective.

Immune checkpoint treatment

To test immune interactions within tumoroids upon perturbation with immune checkpoints inhibitors, individual tumoroids were seeded into 2.5mg/ml collagen gel containing 25 x 10^6/ml splenocytes isolated from CAG.egfp mice. After polymerization in 8 well chamber Borosilicate coverglass slides (Lab-tek), the samples were treated with either 20µg/ml anti-CTLA4 (BE0164, Bio X Cell) or IgG control for 48 hours with daily exchange of media and live imaged.

Live cell imaging and image analysis

To study immune cell migration in 3D collagen gels in the presence of the tumoroid we performed live-cell imaging experiments with a Zeiss Z1 AxioObserver equipped with an environmental chamber to maintain cells at 37C and 5% CO2 humidified atmosphere while imaging. The tumoroids were imaged with 20x objective, both in control wells and wells with α-CTLA4 treatment, in at least 3 fields of view at the edge of the printed structure every 8

mins for a total duration of 48h. To analyse, individual cells from the videos generated were detected together with their movement tracks using Trackmate, an open-source plugin for ImageJ. Quantification of tumoroid area and shape was performed in ImageJ. The ratio of minimum:maximum axis length was used as an approximation of sphericity and centre coordinates.

To monitor cell migration relative to the tumoroid, a home-written python code (Supplementary Information) was used to analyse the distance between cells and the center of tumoroid during their tracking durations. In general, the center coordinates of the tumoroid (x_0, y_0) were first checked using ImageJ. Afterward, columns containing cell ID, x coordinate, y coordinate, and frame number were extracted from the csv file generated by Trackmate. For every cell at each given tracking frame, the cell-to-center distance (D) was calculated using the following equation, where (x_{nm}, y_{nm}) defines the x,y coordinates of cell n at the m^{th} frame.

$$D = \sqrt{(x_{nm} - x_0)^2 + (y_{nm} - y_0)^2}$$

Intensity plots were then generated using cell-to-center distances versus corresponding time points in the total tracking duration.

Statistical analysis

To evaluate statistical significance between two samples a T-test was performed. For multiple comparisons, a one-way ANOVA was employed with a Dunnett or Tukey post- hoc test. Data are expressed as median or mean ± SEM. Data were analysed using Graphpad Prism 9 Software packages

3 **Results**

The deployable 3D bioprinter

The deployable and portable features of our 3D bioprinter are highlighted in Figure 1A. Here, an in-house printhead was designed and built to be mounted on a foldable supporting frame, with a robotic arm performing the printing motions while holding the stage. Driven by a stepper motor, the extrusion-based printhead provides 0.8 µm per step dispensing accuracy.

By tuning the extrusion rate and robotic arm moving speed, this printer can reach a printing resolution of around 150 μm, which is adequate for retaining as-printed cell viability and creating the tumoroid core-shell features. Comparing to traditional 3-axis linear stages-based dispensing systems, our design offers better compactness which enables it to be folded into a highly packed form. The folded deployable printer is light-weight, and can be easily reassembled within 15 minutes, making the switching process user-friendly.

Moreover, the programmable robotic arm [22] provides flexibility for printing with versatile geometry inputs and performing customised functions based on python codes. A home-written function used here for tumoroid printing is the position calibration at user-defined step size, which offers opportunity to check and fine tune the core printing position. This function ensured the cancer core was deposited at the desired location and helped to overcome any position deviations caused by positioning error of the robotic arm (±0.2mm), ensuring repeatability. For the hardware, various 3D-printed stages can be attached to the robotic arm, including stages for glass slides and petri dishes, allowing more freedom on using custom-designed receivers.

Overall, with the deployable design, this printer can readily adapt to different working environments including tissue-culture hoods, while preserving relatively high accuracy. Here, the deployable printer demonstrated an integration of space adaptability, customization flexibility and biological relevance (see further results below), which has not yet been shown by existing open-source bioprinters that cost below £1,000 [24,25,26,21]. We foresee this deployable 3D bioprinter as a promising, user-friendly tool to make bioprinting accessible to a wider research community.

Optimization of tumoroids with a core-shell structure

To construct tumoroids with a core-shell structure, stromal cells laden in a bioink containing gelatin and alginate were printed first in a block shape, and the cancer compartment was subsequently extruded into the stromal-bioink block after repositioning the needle at the center of the block (Figure 1B, and model procedure in Supplementary video-1). While the thermo-crosslinkable nature of gelatin provided the bio-ink with enough mechanical strength to hold its own weight during printing, Ca^{2+} ions crosslinking within alginate helped to maintain the shape of the structure during post-printing culture. A home-written Python code was used to enable position calibration along x, y, z directions during core printing, which

helped ensure the cancer compartment was centrally deposited. Core-shell structures generated could be printed to a total approximate size of 2mm x 2mm x 2mm, containing central cores of 1mm x 1mm x 1mm. The average printing time per tumoroid is approximately 90 s.

After printing and cross-linking, tumoroids were maintained in agarose-coated 12-well plates to support reproducibility in size and shape between each tumoroid (Figure 1B). On day 2, alginate lyase treatment was performed. This was a crucial post-printing step that determined the final shape of tumoroids. The concentration of alginate lyase was a key factor that affect the outcome of lyase treatment. A slight reduction in tumoroid volume was observed with increasing alginate lyase concentration (Figure 2A-D). However, despite slight dimensional shrinkage, a more uniform, spherical structure was obtained with higher concentrations of 340μg/ml, compared with irregular morphologies generated with lower lyase concentrations, (Figure 2E&F). To prevent tumoroid collapse after lyase treatment (Figure 2D), and to ensure mechanically robust tumoroids with desired morphology, we operated with $1.7x10^8$cells/ml in the bio-ink, ensuring that cell-laden gels were mixed gently during the printing process. After this initial optimization, subsequent experiments were performed using $1.7x10^8$cells/ml followed by 340μg/ml alginate lyase treatment for 24h on day 2 to enable generation of robust, reproducible tumoroids.

Printed tumoroids reflect features of the *in vivo* tumor microenvironment

As the 3D printed tumoroids showed good reproducibility in shape and size after printing and crosslinking at the macroscopic level, the core-shell structure formed after alginate removal was examined by confocal imaging after cryosectioning. Figure 3A&B showed that the tumoroids generated contained both CAFs and tumor cells, and a clear core-shell structure was present with CAFs forming a defined capsule, but CAFs were also observed to have infiltrated throughout the mass core (Figure 3B), which was seen *in vivo*. Deposition of ECM components such as Collagen I, Osteopontin and Perlecan could be detected, indicative of CAF functionality (Figure 3C). *In vivo*, CAFs represent at heterogenous population [27] [28]. However, in long-term culture, fibroblasts adapt to 2D culture conditions losing phenotypic and functional heterogeneity and becoming dominated by αSMA-expressing fibroblasts. To test if tumoroids could more accurately recapitulate *in vivo* conditions, we compared expression of two CAF markers from 2D co-culture, 3D printed tumoroids, and those

harvested from day 11 tumors grown *in vivo*. Figure 3D&E showed that *in vivo*, a mix of $CD34^+$ and αSMA^+ expressing CAFs was measured; however, on a 2D culture, CAFs predominantly expressed αSMA with $CD34^+$ populations barely detectable. In comparison, tumoroids exhibited a mix of $CD34^+$ and SMA^+ CAF, with the re-emergence of $CD34^+$ populations more reminiscent of *in situ* tumors. Thus, the *in vitro* environment generated in mixed tumoroids represents a favorable platform to study events and interactions occurring within a tumor.

Inclusion of immune cells in simulated extracellular matrices

To further mimic the *in vivo* situation, a mixed population of splenocytes was dispersed in a collagen gel, where the tumoroid was further embedded within. Live imaging revealed that intratumoral immune cells were rapidly recruited from the surrounding extracellular matrix (ECM) (Supplementary video-2). Flow cytometry confirmed that diverse immune cell populations were associated with tumoroid structures (Figure 4A and Supplementary Figure 1A), revealing the presence of infiltrating T cells, NK and $CD11b^+$ cells, and where T cells represented one of the most dominant populations identified. The pattern of infiltration of *in vitro* tumoroids was not dissimilar to those measured at different time points of pancreatic tumors *in vivo* (Figure 4B). In both cases, a clear T cell population could be detected. However, *in vivo*, we noted an elevated proportion of $CD11b^+$ cells, while "other" cells dominated *in vitro*. This likely reflects the input pool of cells utilized *in vitro*, since isolated splenocytes are particularly rich in B cells compared with myeloid populations. This may be overcome with initial selection steps during tissue processing. Importantly, as reported for many tumor types, confocal imaging of the *in vitro* culture sections confirmed that CD11b-expressing myeloid populations penetrated deep within the tumoroid (Figure 4C, white colored cells).

Immunotherapy perturbation of multi-compartmental tumoroids

To determine if bioprinted, compartmental tumoroids can be applied to test potential therapies as part of drug discovery pipelines, we then perturbed the system by treating with the immune checkpoint inhibitor anti-CTLA4. Tumoroids and labelled splenocytes were allowed to equilibrate for 12 hours before addition of anti-CTLA4 or control IgG (Figure 5A-C). Live imaging confirmed rapid homing of immune cells to tumoroids (Supplementary video- 2&3). Figure 5D shows flow cytometry detection of splenocytes associated with the tumoroid after 48h incubation. While no significant increase in the total counts of infiltrating

$CD45^+$ cells and $CD8^+$ cells were observed in the period tested, the behavior of splenocytes was significantly different between IgG control and anti-CTLA4 treatments. Quantification of cell migration from the captured videos showed that immune cells stimulated with immunotherapy moved noticeably faster (Figure 5E&F), and covered a greater distance measured by displacement to get there (Figure 5G&H), indicative of a more direct homing path compared with IgG control treated conditions. Indeed, further analysis of immune cell displacement relative to the center of tumoroid revealed an increased immune cell directionality towards tumoroid in anti-CTLA4 treated groups (Figure 5I). While an initial burst of movement towards tumoroids was observed in IgG controls, after 200 minutes this stalled, with a high density of cells remaining between 900-1000 microns from the tumoroid center. In contrast, directional homing of cells was maintained for the duration of the experiment when in the presence of anti-CTLA4. Of note, between 400 and 600 minutes, a sizable proportion of cells were observed approximately 700 microns away from the center. Beyond this time point, cell displacement became more randomly distributed. Considering the radius of the tumoroid is approximately 700 microns, this loss of directionality may be a consequence of immune cells reaching the tumoroid surface, where the cells could change their behavior from directed migration to infiltration of the mass.

4 Discussion

Here we utilized 3D bioprinting to generate core-shell tumoroids. We showed that with this approach, reproducible tumour masses surrounded and punctuated throughout by CAF networks and *de novo* synthesized ECM, could be readily achieved. Addition of immune cells to the core-shell tumoroids, which homed and infiltrated the mass, added an additional compartment to recapitulate the complexities of the tumour microenvironment. Tumoroids could then be applied to examine therapy responses, in this case, anti-CTLA4 immune therapy. Importantly, the bioArm and set-up were designed to be affordable, and mobile to allow easy transportation between laboratories within a bag, thereby enabling greater accessibility to researchers outside of more specialized engineering disciplines whilst retaining printing resolution of around 150 µm.

Optimization of printing conditions identified that higher concentrations of alginate lyase were needed to generate structures uniform in shape, and reliably spherical. Without alginate

lyase treatment, structures were irregular in size and shape, looser, and lost cells into the surrounding media. It is possible that long-term inclusion of crosslinked alginate between cells was sufficient to inhibit cell-cell interactions, resulting in the loosely packed clusters observed. In contrast, the alginate lyase treatment, and the removal of alginate from the system supported stronger cell-cell interactions and the formation of compacted tissues more closely resembling the dense nature of tumors *in vivo*.

The TME contains diverse cell types including CAFs, immune cells, and endothelial cells embedded in the ECM. The complex milieu of soluble factors and ECM composition modulates biophysical and biochemical traits of the tumor e.g. hypoxia, acidity, and bioavailability, alongside physical exclusion of infiltrating cells. Together, these constituents and the traits they convey within the TME facilitate disease progression but can also modulate impact the efficacy or response to treatment [29], [30]. Even in 2D co-culture systems, inclusion of fibroblasts is sufficient to negate the cytotoxic effect of conventional chemotherapeutic drugs [31,32,33]. Thus, there has been an intense effort to develop more complex model systems to recapitulate the tumor setting. These include hanging drop cultures, spheroids, and microfluidic set-ups which have evolved from monocultures within 3D microenvironments towards inclusion of multiple cell types that simulate the different tumor compartments. Such models have shown the importance of cross compartment communication on cell behavior, and drug efficacy [34], [35]. Alongside, patient derived organoid systems have been implemented to examine therapy approaches and drug combinations in multiple cancer types [36], [37], [38], [39]. Unlike cell lines, organoids maintain a heterogenous genetic landscape, but culture conditions tend to select against less rapidly dividing populations, and stromal constituents are frequently lost [40]. Thus, tumoroids represent a viable alternative that has adequate throughput and incorporates multiple cell types such as CAFs and immune cells to recapitulate the TME.

Our approach, which rapidly and robustly produces core-shell structures of murine tumors, may be developed to incorporate patient samples which maintain genetic heterogeneity, alongside stromal populations. While a clear CAF shell surrounded the tumor mass, a CAF network could also be seen deep within the core of tumoroids. Tumoroid associated CAFs started to display a greater degree of heterogeneity more akin to *in vivo* situations compared with 2D cultures [27], [28]. This increase in CAF diversity may continue to further develop in longer-term cultures. Moreover, as some tumor types exhibit dense stromal swathes between

tumor nests *in vivo*, in the future it may also be possible to embed multiple adjacent tumoroids within a collagen gel to recreate the stromal rich phenotype on a larger scale. Immune cells within the tumoroid environment homed to tumoroids, with populations such as CD11b-expressing cells infiltrating into the core consistent with reports across multiple tumor types [42], [43], [41]. We then showed that core-shell tumoroids could be used as a platform to test immunotherapies. While in the time periods examined, we did not detect significant treatment-induced immune activation of infiltrating splenocytes, anti-CTLA4 enhanced the speed and directionality of immune cell migration towards tumoroids. These observations are consistent with *in vivo* studies in murine breast cancer and melanoma tumors which also reported significantly enhanced motility of tumor infiltrating lymphocytes [44], [45].

In summary, we have shown here the development of a low cost, deployable extrusion bioprinting workflow capable of robustly generating tumoroids that lead to multiple compartments of the tumor microenvironment. The portability and ease of use of the robotic arm offers the potential to significantly widen the accessibility of 3D bioprinting for gaining mechanistic understanding of TME interactions, and for future development of cancer drug testing approaches.

5 References

1. Ferlay, J. *et al.* Cancer statistics for the year 2020: An overview. *Int J Cancer* **149**, 778–789 (2021).
2. Sung, H. *et al.* Global Cancer Statistics 2020: GLOBOCAN Estimates of Incidence and Mortality Worldwide for 36 Cancers in 185 Countries. *CA: A Cancer Journal for Clinicians* **71**, 209–249 (2021).
3. Giraldo, N. A. *et al.* The clinical role of the TME in solid cancer. *British Journal of Cancer 2018 120:1* **120**, 45–53 (2018).
4. Tang, H., Qiao, J. & Fu, Y. X. Immunotherapy and tumor microenvironment. *Cancer Letters* **370**, 85–90 (2016).
5. Li, R. *et al.* Macrophage-Secreted TNFα and TGFβ1 Influence Migration Speed and Persistence of Cancer Cells in 3D Tissue Culture via Independent Pathways. *Cancer Research* **77**, 279–290 (2017).

6. Sung, K. E. *et al.* Transition to invasion in breast cancer: a microfluidic in vitro model enables examination of spatial and temporal effects. *Integrative Biology* **3**, 439–450 (2011).
7. Katt, M. E., Placone, A. L., Wong, A. D., Xu, Z. S. & Searson, P. C. In Vitro Tumor Models: Advantages, Disadvantages, Variables, and Selecting the Right Platform. *Frontiers in Bioengineering and Biotechnology* **4**, (2016).
8. Below, C. R. *et al.* A microenvironment-inspired synthetic three-dimensional model for pancreatic ductal adenocarcinoma organoids. *Nature Materials 2021 21:1* **21**, 110–119 (2021).
9. Pepelanova, I., Kruppa, K., Scheper, T. & Lavrentieva, A. Gelatin-Methacryloyl (GelMA) Hydrogels with Defined Degree of Functionalization as a Versatile Toolkit for 3D Cell Culture and Extrusion Bioprinting. *Bioengineering 2018, Vol. 5, Page 55* **5**, 55 (2018).
10. Rebelo, S. P. *et al.* 3D-3-culture: A tool to unveil macrophage plasticity in the tumour microenvironment. *Biomaterials* **163**, 185–197 (2018).
11. Jeong, S. Y., Lee, J. H., Shin, Y., Chung, S. & Kuh, H. J. Co-Culture of Tumor Spheroids and Fibroblasts in a Collagen Matrix-Incorporated Microfluidic Chip Mimics Reciprocal Activation in Solid Tumor Microenvironment. *PLOS ONE* **11**, e0159013 (2016).
12. Day, C. P., Merlino, G. & van Dyke, T. Preclinical Mouse Cancer Models: A Maze of Opportunities and Challenges. *Cell* **163**, 39–53 (2015).
13. Qin, X. *et al.* Cell-type-specific signaling networks in heterocellular organoids. *Nature Methods 2020 17:3* **17**, 335–342 (2020).
14. Hum, N. R. *et al.* Comparative Molecular Analysis of Cancer Behavior Cultured In Vitro, In Vivo, and Ex Vivo. *Cancers (Basel)* **12**, (2020).
15. Langer, E. M. *et al.* Modeling Tumor Phenotypes In Vitro with Three-Dimensional Bioprinting. *Cell Reports* **26**, 608-623.e6 (2019).
16. Neal, J. T. *et al.* Organoid Modeling of the Tumor Immune Microenvironment. *Cell* **175**, 1972-1988.e16 (2018).
17. Zhou, X. *et al.* 3D Bioprinting a Cell-Laden Bone Matrix for Breast Cancer Metastasis Study. *ACS Applied Materials and Interfaces* **8**, 30017–30026 (2016).
18. Ioannidis, K. *et al.* A Custom Ultra-Low-Cost 3D Bioprinter Supports Cell Growth and Differentiation. *Frontiers in Bioengineering and Biotechnology* **8**, 1279 (2020).

19. Pusch, K., Hinton, T. J. & Feinberg, A. W. Large volume syringe pump extruder for desktop 3D printers. *HardwareX* **3**, 49–61 (2018).
20. Hakimi, N. *et al.* Handheld skin printer: in situ formation of planar biomaterials and tissues. *Lab on a Chip* **18**, 1440–1451 (2018).
21. Ying, G. *et al.* An open-source handheld extruder loaded with pore-forming bioink for in situ wound dressing. *Materials Today Bio* **8**, 100074 (2020).
22. Lei, I. M., Sheng, Y., Lei, C. L., Leow, C. & Huang, Y. Y. S. A hackable, multi-functional, and modular extrusion 3D printer for soft materials. (2022) doi:10.48550/arxiv.2203.07497.
23. Munir, H. *et al.* Stromal-driven and Amyloid β-dependent induction of neutrophil extracellular traps modulates tumor growth. *Nature Communications 2021 12:1* **12**, 1–16 (2021).
24. Hinton, T. J. *et al.* Three-dimensional printing of complex biological structures by freeform reversible embedding of suspended hydrogels. *Science Advances* **1**, (2015).
25. Reid, J. A. *et al.* Accessible bioprinting: adaptation of a low-cost 3D-printer for precise cell placement and stem cell differentiation. *Biofabrication* **8**, 025017 (2016).
26. Kahl, M., Gertig, M., Hoyer, P., Friedrich, O. & Gilbert, D. F. Ultra-low-cost 3D bioprinting: Modification and application of an off-the-shelf desktop 3D-printer for biofabrication. *Frontiers in Bioengineering and Biotechnology* **7**, 184 (2019).
27. Davidson, S. *et al.* Single-Cell RNA Sequencing Reveals a Dynamic Stromal Niche That Supports Tumor Growth. *Cell Reports* **31**, (2020).
28. Elyada, E. *et al.* Cross-species single-cell analysis of pancreatic ductal adenocarcinoma reveals antigen-presenting cancer-associated fibroblasts. *Cancer Discovery* **9**, 1102–1123 (2019).
29. Qiao, Y. *et al.* IL6 derived from cancer-associated fibroblasts promotes chemoresistance via CXCR7 in esophageal squamous cell carcinoma. *Oncogene 2018 37:7* **37**, 873–883 (2017).
30. Zhang, D. *et al.* Tumor–Stroma IL1b-IRAK4 feedforward circuitry drives tumor fibrosis, chemoresistance, and poor prognosis in pancreatic cancer. *Cancer Research* **78**, 1700–1712 (2018).
31. Straussman, R. *et al.* Tumour micro-environment elicits innate resistance to RAF inhibitors through HGF secretion. *Nature 2012 487:7408* **487**, 500–504 (2012).

32. Cheteh, E. H. *et al.* Human cancer-associated fibroblasts enhance glutathione levels and antagonize drug-induced prostate cancer cell death. *Cell Death & Disease 2017 8:6* **8**, e2848–e2848 (2017).
33. Luraghi, P. *et al.* MET signaling in colon cancer stem-like cells blunts the therapeutic response to EGFR inhibitors. *Cancer Research* **74**, 1857–1869 (2014).
34. Langhans, S. A. Three-dimensional in vitro cell culture models in drug discovery and drug repositioning. *Frontiers in Pharmacology* **9**, 6 (2018).
35. Sufi, J. *et al.* Multiplexed single-cell analysis of organoid signaling networks. *Nature Protocols 2021 16:10* **16**, 4897–4918 (2021).
36. Driehuis, E., Kretzschmar, K. & Clevers, H. Establishment of patient-derived cancer organoids for drug-screening applications. *Nature Protocols 2020 15:10* **15**, 3380–3409 (2020).
37. Vlachogiannis, G. *et al.* Patient-derived organoids model treatment response of metastatic gastrointestinal cancers. *Science (1979)* **359**, 920–926 (2018).
38. Kopper, O. *et al.* An organoid platform for ovarian cancer captures intra- and interpatient heterogeneity. *Nature Medicine 2019 25:5* **25**, 838–849 (2019).
39. Mazzocchi, A. R., Rajan, S. A. P., Votanopoulos, K. I., Hall, A. R. & Skardal, A. In vitro patient-derived 3D mesothelioma tumor organoids facilitate patient-centric therapeutic screening. *Scientific Reports 2018 8:1* **8**, 1–12 (2018).
40. Sachs, N. *et al.* A Living Biobank of Breast Cancer Organoids Captures Disease Heterogeneity. *Cell* **172**, 373-386.e10 (2018).
41. Duhan, V. & Smyth, M. J. Innate myeloid cells in the tumor microenvironment. *Current Opinion in Immunology* **69**, 18–28 (2021).
42. Tsujikawa, T. *et al.* Quantitative Multiplex Immunohistochemistry Reveals Myeloid-Inflamed Tumor-Immune Complexity Associated with Poor Prognosis. *Cell Reports* **19**, 203–217 (2017).
43. Liudahl, S. M. *et al.* Leukocyte heterogeneity in pancreatic ductal adenocarcinoma: Phenotypic and spatial features associated with clinical outcome. *Cancer Discovery* **11**, 2014–2031 (2021).
44. Pentcheva-Hoang, T., Simpson, T. R., Montalvo-Ortiz, W. & Allison, J. P. Cytotoxic T lymphocyte antigen-4 blockade enhances antitumor immunity by stimulating melanoma-specific T-cell motility. *Cancer Immunol Res* **2**, 970–980 (2014).

45. Ruocco, M. G. *et al.* Suppressing T cell motility induced by anti–CTLA-4 monotherapy improves antitumor effects. *The Journal of Clinical Investigation* **122**, 3718–3730 (2012).

6 Figure Legends

Figure 1. Deployable extrusion bioprinting to create a core-shell tumoroid. A) The deployable bioprinter can be folded, transported, and rapidly re-assembled for printing inside a biosafety cabinet. **B)** Schematic of the printing working flow from tumoroid printing (i, ii, iii), enzymatic treatment (iv, v) through to immune interaction (vi).

Figure 2. Alginate lyase treatment optimization for pancreatic cancer core-shell tumoroids. Representative brightfield tile scan images of tumoroids receiving **A)** no lyase, **B)** 170 μg/ml alginate lyase, **C)** 340 μg/ml and **D)** 340 μg/ml with low cell concentration <1.5 x 10^8cells/ml. Quantification of **E)** tumoroid area and **F)** sphericity following treatment with different concentrations of alginate lyase. **G)** Flow cytometry quantification of tumoroid viability with or without alginate lyase. **H)** Flow cytometry quantification of CAF frequency within tumoroids with and without alginate lyase treatment. Scale bars, 200 μm.

Figure 3. Tumoroid CAFs show in vivo-like characteristics. A) Representative confocal image of a CAF capsule tumoroid phenotype. CAFs (PDGFRα, green); nuclei (DAPI, blue). **B)** Representative confocal images of tumoroid sections showing a CAF network phenotype deep within the tumoroid core. Inset i: higher power image of the CAF shell. Inset ii: higher power magnification of CAF-core network. **C)** Representative confocal image depicting *de novo* extracellular matrix deposition within the tumoroid. Merged and individual channels for Perlecan (green), Osteopontin (white), Collagen I (red) and nuclei (blue) are shown. Inset shows a higher power field of ECM at the tumoroid periphery. **D)** Flow cytometric

quantification of the proportion of $CD34^+$ or αSMA^+CAFs from 2D and 3D cultures, and *in vivo* settings. Scale bars, 190 μm **(A)**, 140 μm **(B, C)**, 36 μm (**C** inset).

Figure 4. Immune cells infiltrate tumoroids as *in vivo*. A) Flow cytometric quantification of tumoroid-infiltrating immune cells (T cells, NK cells, $CD11b^+$ and others; shown as percentage of $CD45^+$ cells). **B)** Flow cytometric quantification of tumor-infiltrating immune cells (T cells, NK cells, $CD11b^+$ and others) detected in mM1 pancreatic tumors *in vivo* at day 7 and day 11. **C)** Representative Confocal images of tumoroid sections after 48h incubation with splenocytes showing $B220^+$ B cells (green) and $CD11b^+$ myeloid cells (white). Inset i, higher power image of leukocytes at the tumoroid periphery; arrowheads denote B cells. Inset ii; higher power view of leukocytes deeper within the core. Scale bars, 36 μm.

Figure 5. Rapid immune cell recruitment to tumoroids following immunotherapy treatment. A-B) Representative tile scan snapshots of tumoroids cultured in a GFP^+ splenocyte-laden collagen I gel at **A)** t=0, **B)** at 48h with IgG control or αCTLA4 treatment. **C)** Close-up fields of the tumoroid images edges after 48h with IgG control or αCTLA4 treatment. **D)** number of infiltrating immune cells (left) and $CD8^+$ T cells (right) per tumoroid. **E-I)** Quantification of immune cell behavior from live imaged movies using the Trackmate ImageJ plugin. Mean speed **(E)**, maximum track speed **(F)**, displacement **(G)** and total distance travelled **(H)** were measured with and without αCTLA4 treatment. **I)** Directionality heatmap shows number of cell tracks over time and their distance from the center of the tumoroid. Scale bars, 200 μm **(A-B)** and 50 μm **(C)**.

Supplementary figure/movie legends

Supplementary Figure 1. A) Flow cytometry quantification of splenocyte populations associated with the tumoroid after 48h treatment with IgG control or αCTLA4. $CD4^+$ and $CD8^+$ T cells, NK cells, $cd11b^+$, B cells, and others; shown as percentage of $CD45^+$ cells.

Supplementary Information

Home-written Python code used to analyze tracking data of single cells movement towards the centre of the tumoroid.

Supplementary video 1

3D bioprinting of a core-shell structure. The yellow ink represents the stromal compartment and the black ink the cancer core.

Supplementary video 2

Immune infiltration of splenocytes (in green) embedded in a collagen I hydrogel towards the bioprinted tumoroid (IgG control).

Supplementary video 3

Immune infiltration of splenocytes (in green) embedded in a collagen I hydrogel towards the bioprinted tumoroid (αCTLA4 treatment).

7 Acknowledgement

We thank the funding supports from Medical Research Council core funding (J.S., C.M, L.N.R), European Research Council (Y.Y.S.H, grant number 758865), W.D Armstrong Trust (C.M. and I.M.L), Cambridge Trust and Chinese Scholars Council (Y.S).

A

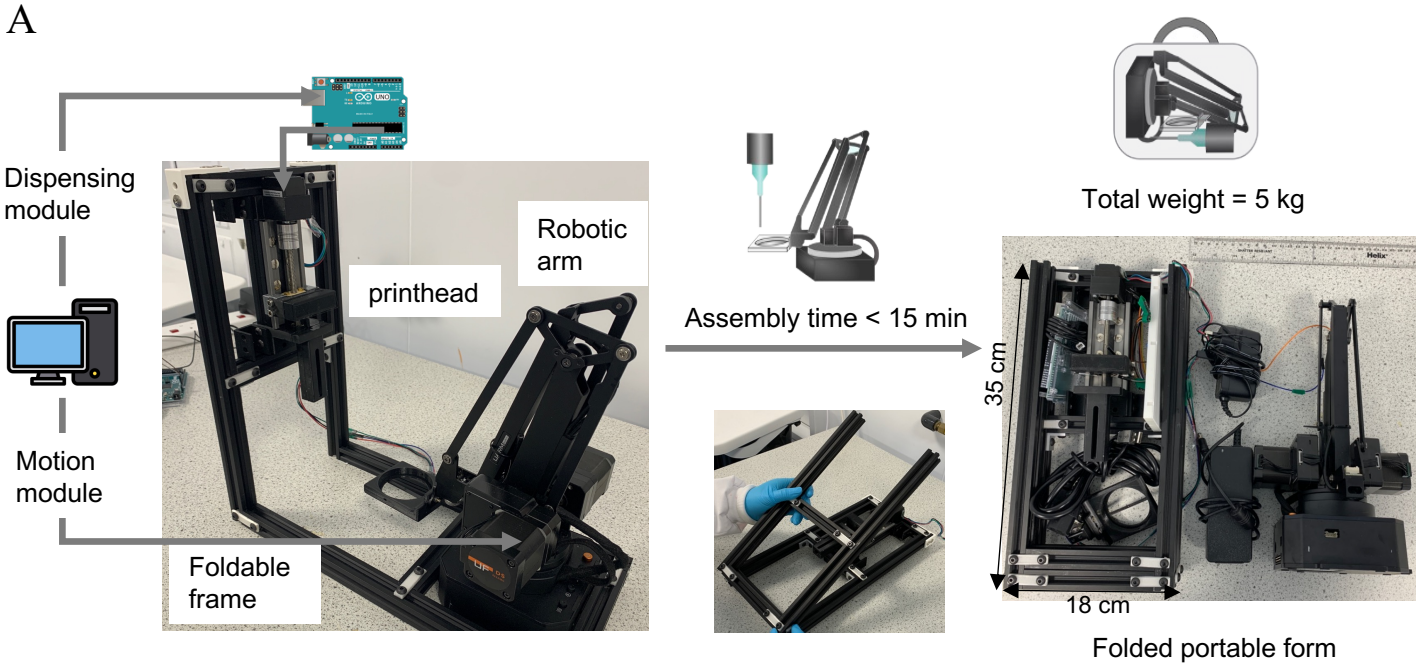

B

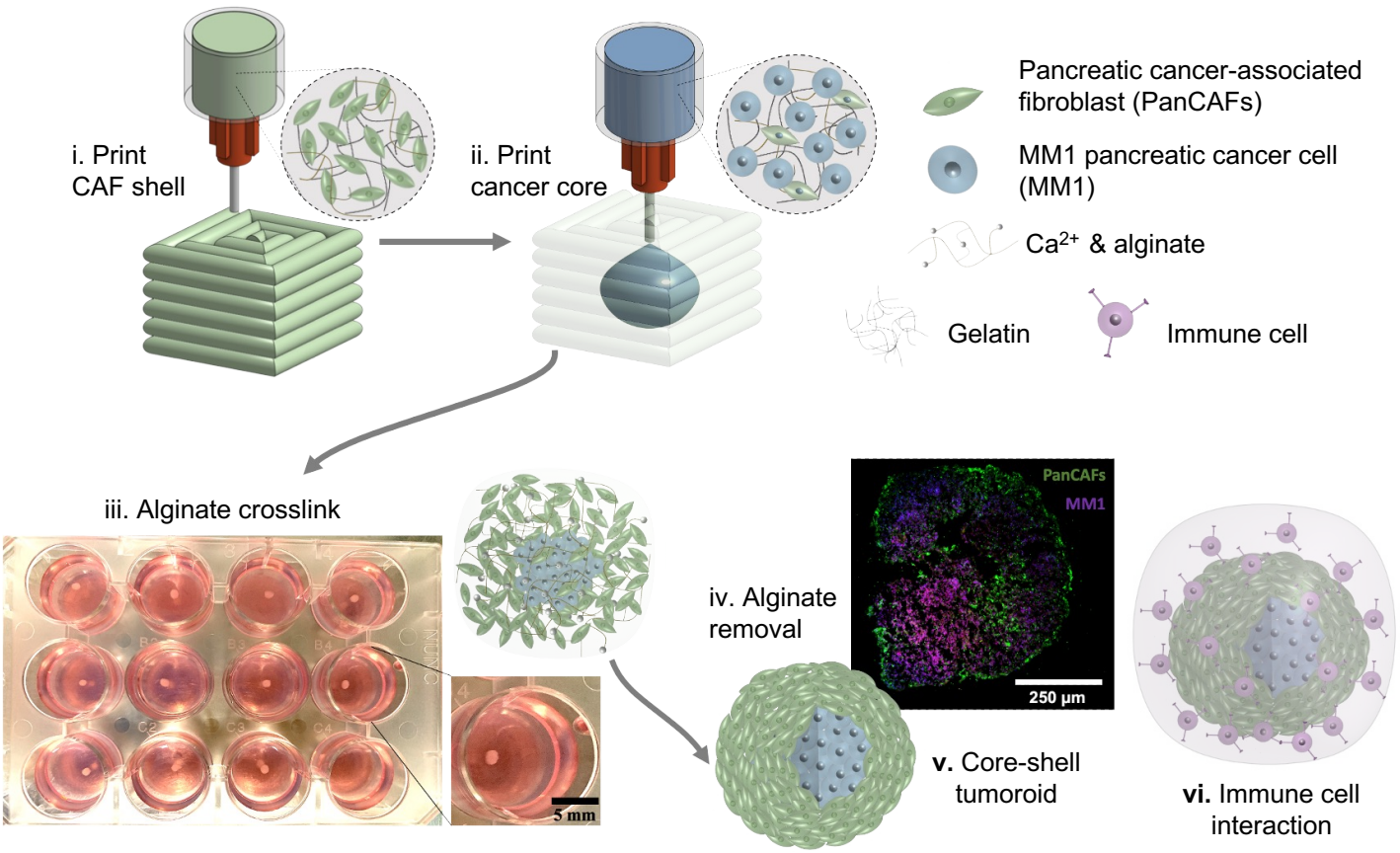

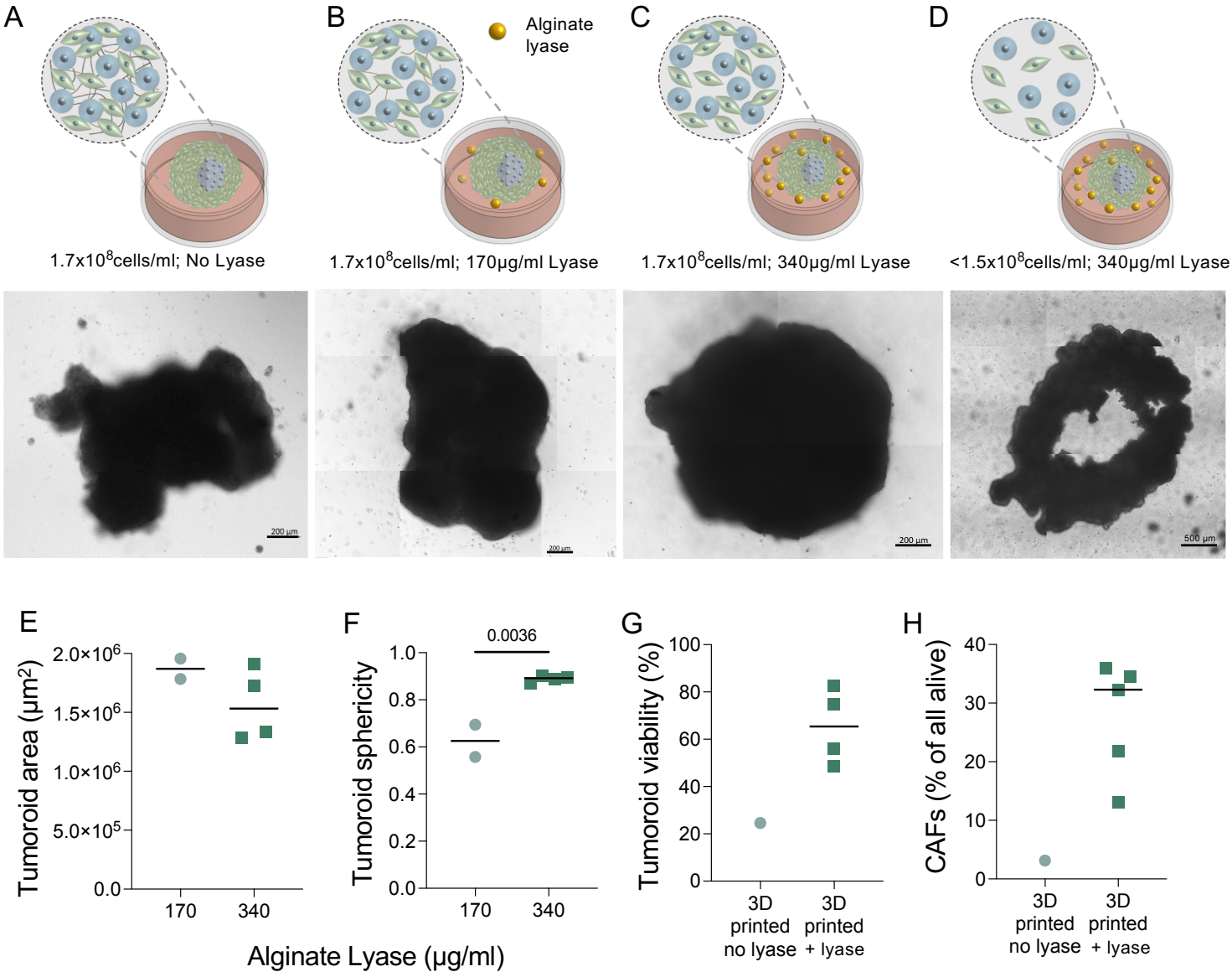
A
B
C
D
Alginate lyase
1.7x10^8cells/ml; No Lyase
1.7x10^8cells/ml; 170µg/ml Lyase
1.7x10^8cells/ml; 340µg/ml Lyase
<1.5x10^8cells/ml; 340µg/ml Lyase
200 µm
200 µm
200 µm
500 µm
E
Tumoroid area (µm²)
2.0×10^6
1.5×10^6
1.0×10^6
5.0×10^5
0.0
170
340
F
Tumoroid sphericity
0.0036
1.0
0.8
0.6
0.4
0.2
0.0
170
340
Alginate Lyase (µg/ml)
G
Tumoroid viability (%)
100
80
60
40
20
0
3D printed no lyase
3D printed + lyase
H
CAFs (% of all alive)
40
30
20
10
0
3D printed no lyase
3D printed + lyase

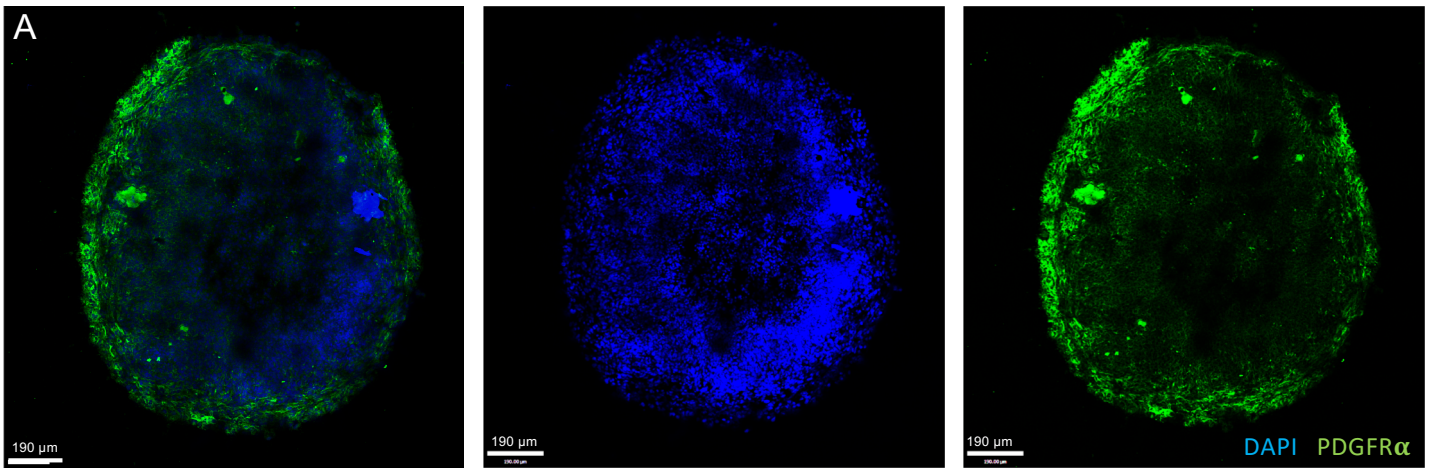
A
190 µm
190 µm
190 µm
DAPI PDGFRα

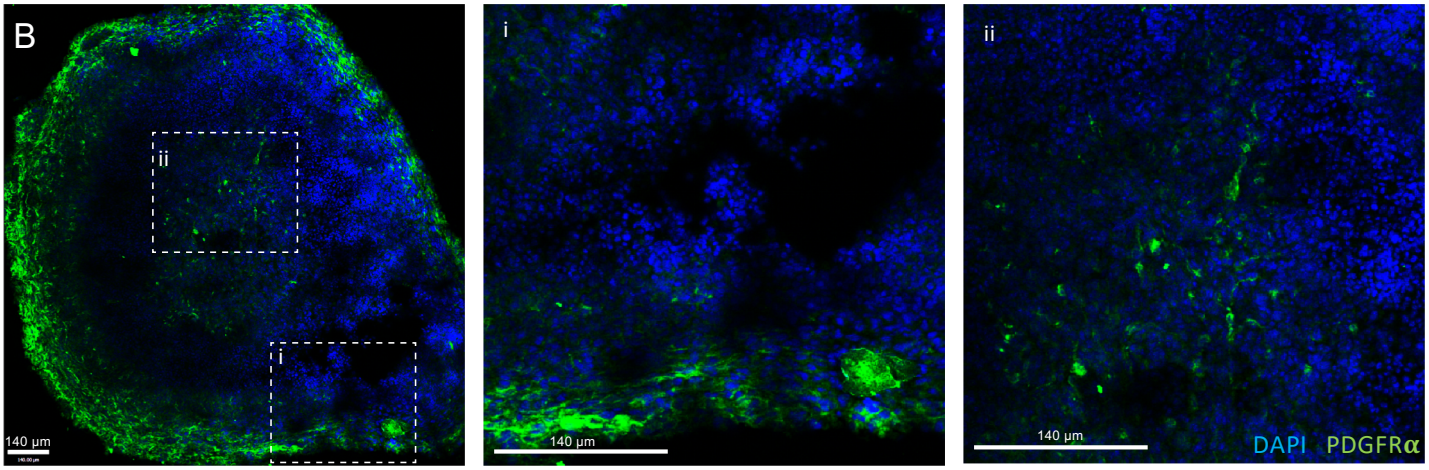
B
ii
i
140 µm
i
140 µm
ii
140 µm
DAPI PDGFRα

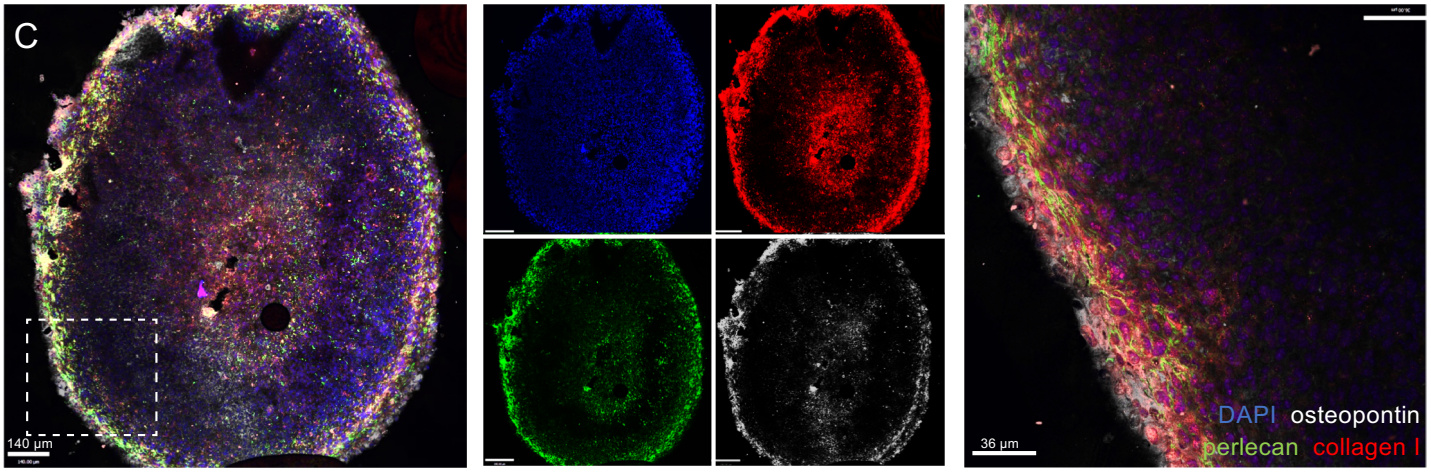
C
140 µm
36 µm
DAPI osteopontin
perlecan collagen I

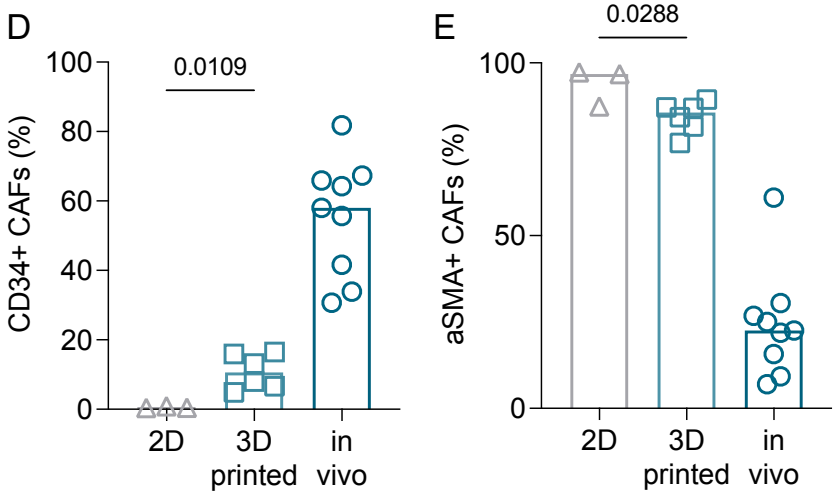
D
0.0109
CD34+ CAFs (%)
100
80
60
40
20
0
2D
3D printed
in vivo

E
0.0288
aSMA+ CAFs (%)
100
50
0
2D
3D printed
in vivo

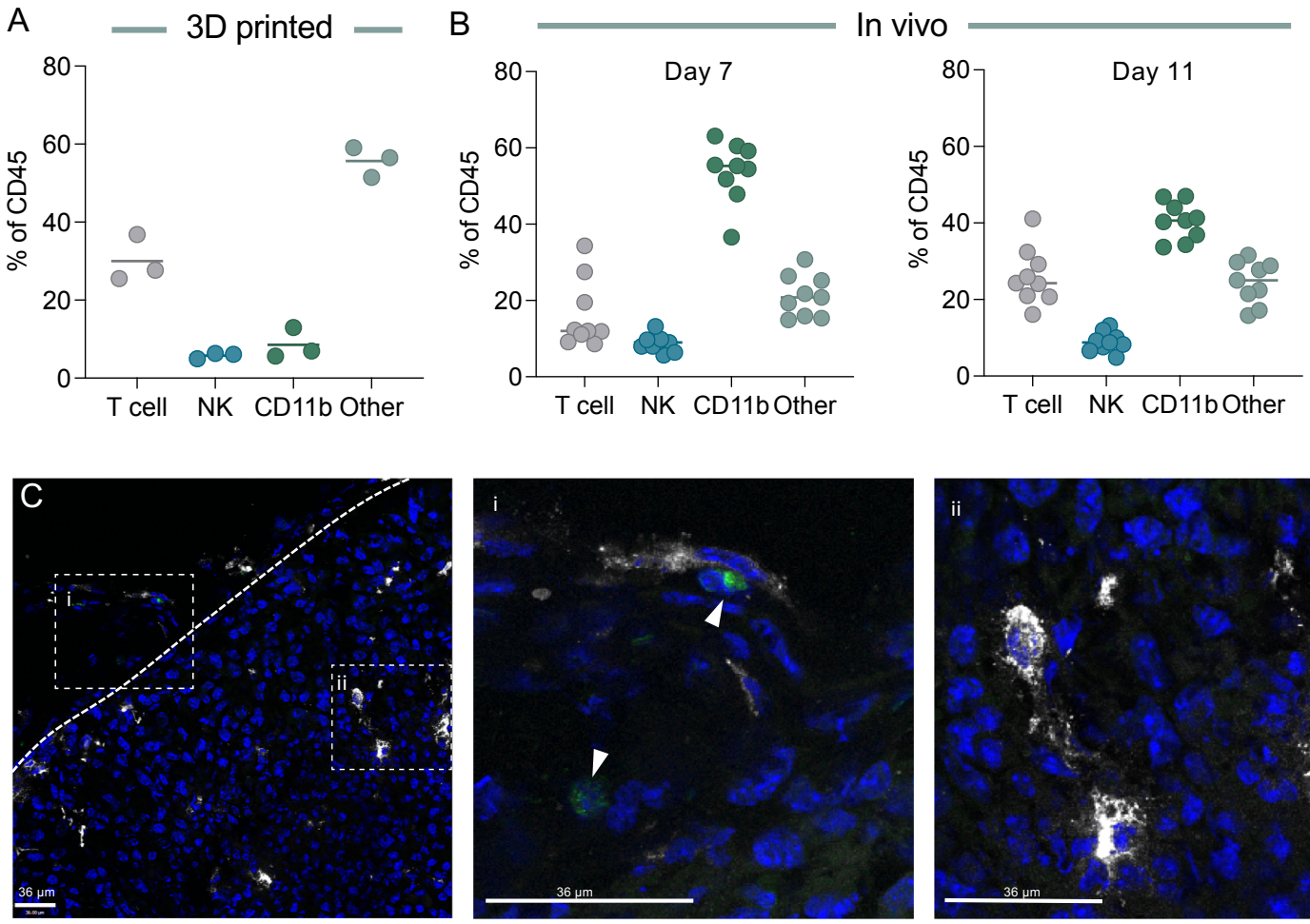
A
3D printed
B
In vivo
Day 7
Day 11
% of CD45
80
60
40
20
0
T cell
NK
CD11b
Other
C
i
ii
36 µm

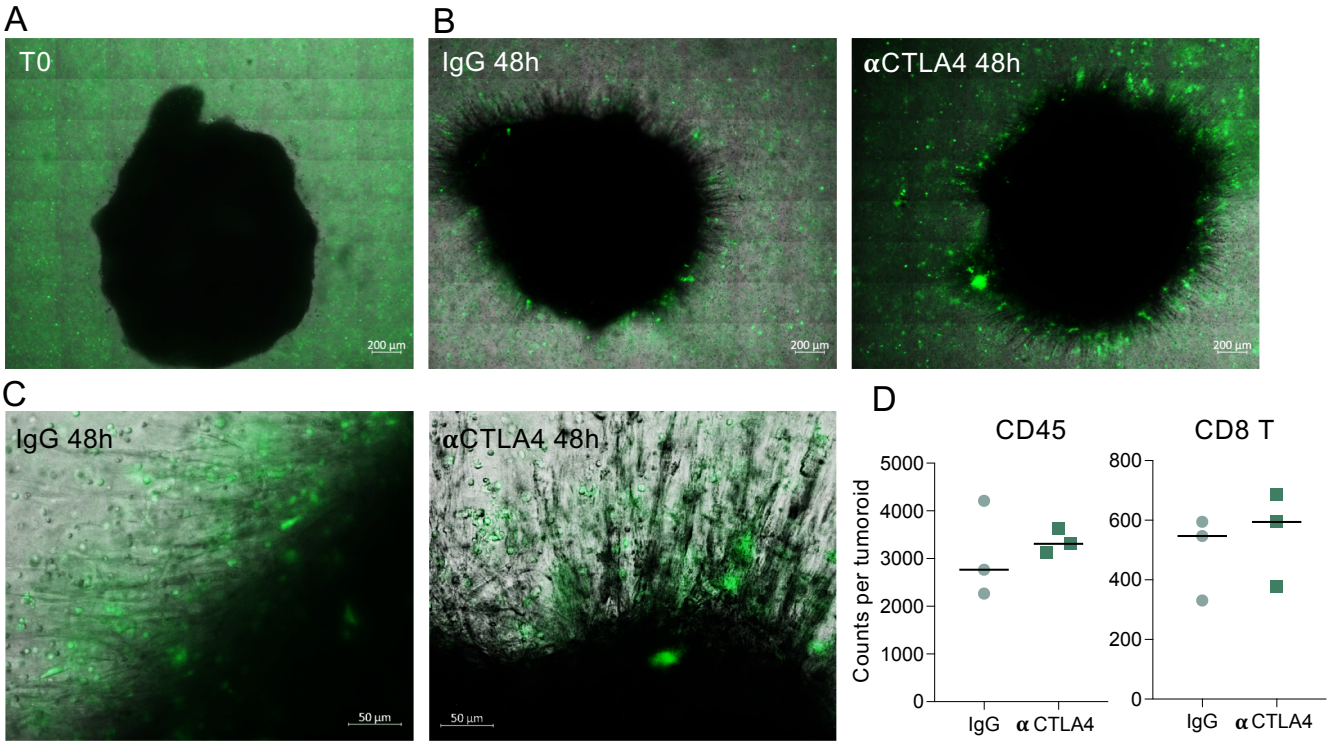
A
T0
200 µm
B
IgG 48h
200 µm
αCTLA4 48h
200 µm
C
IgG 48h
50 µm
αCTLA4 48h
50 µm
D
CD45
CD8 T
Counts per tumoroid
5000
4000
3000
2000
1000
0
800
600
400
200
0
IgG
αCTLA4
IgG
αCTLA4

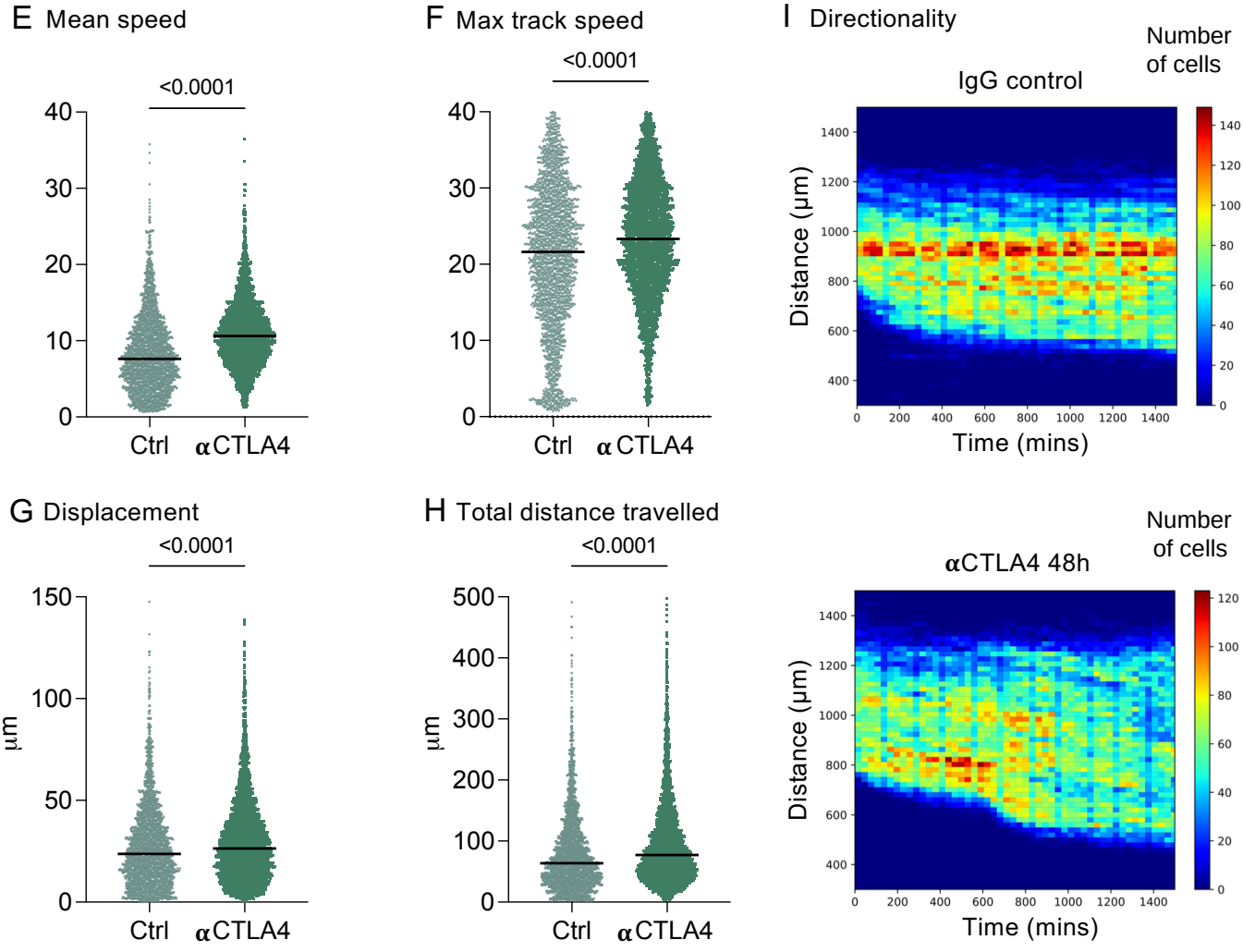
E Mean speed
<0.0001
40
30
20
10
0
Ctrl
αCTLA4
F Max track speed
<0.0001
40
30
20
10
0
Ctrl
αCTLA4
I Directionality
Number of cells
IgG control
Distance (µm)
1400
1200
1000
800
600
400
0
200
400
600
800
1000
1200
1400
Time (mins)
140
120
100
80
60
40
20
0
G Displacement
<0.0001
µm
150
100
50
0
Ctrl
αCTLA4
H Total distance travelled
<0.0001
µm
500
400
300
200
100
0
Ctrl
αCTLA4
Number of cells
αCTLA4 48h
Distance (µm)
Time (mins)
120
100
80
60
40
20
0